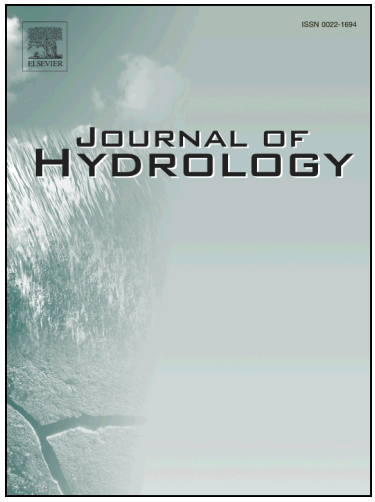


Research papers

# Fluoride and phosphate release from carbonate-rich fluorapatite during Managed Aquifer Recharge

David Schafer, Michael Donn, Olivier Atteia, Jing Sun, Colin MacRae, Mark Raven, Bobby Pejcic, Henning Prommer

PII: S0022-1694(18)30370-6
DOI: https://doi.org/10.1016/j.jhydrol.2018.05.043
Reference: HYDROL 22820

To appear in: *Journal of Hydrology*

Received Date: 1 April 2018
Revised Date: 17 May 2018
Accepted Date: 18 May 2018

Please cite this article as: Schafer, D., Donn, M., Atteia, O., Sun, J., MacRae, C., Raven, M., Pejcic, B., Prommer, H., Fluoride and phosphate release from carbonate-rich fluorapatite during Managed Aquifer Recharge, *Journal of Hydrology* (2018), doi: https://doi.org/10.1016/j.jhydrol.2018.05.043

# Fluoride and phosphate release from carbonate-rich fluorapatite during Managed Aquifer Recharge

*David Schafer [1,2], Michael Donn[3], Olivier Atteia[4], Jing Sun[1,3], Colin MacRae[5], Mark Raven[6], Bobby Pejcic[7] and Henning Prommer[1,2,3 *].*

[1]*University of Western Australia, School of Earth Sciences, Western Australia*

[2]*National Centre for Groundwater Research and Training, Flinders University, Adelaide, GPO Box 2100, SA 5001, Australia*

[3]*CSIRO Land and Water, Private Bag No. 5, Wembley, Western Australia, 6913*

[4]*ENSEGID, Université de Bordeaux, 1 Allee Daguin, 33607 Pessac Cedex, France*

[5]*CSIRO Mineral Resources, Private Bag No. 10, Clayton South, Victoria, 3169*

[6]*CSIRO Land and Water, Locked Bag 2, Glen Osmond, South Australia*

[7]*CSIRO Energy, 26 Dick Perry Ave, Kensington, Western Australia, 6151*

** Corresponding Author*

*Phone: +61 8 93336272; email: Henning.Prommer@csiro.au*

**Submitted to *Journal of Hydrology***

## Abstract

Managed aquifer recharge (MAR) is increasingly used as a water management tool to enhance water availability and to improve water quality. Until now, however, the risk of fluoride release during MAR with low ionic strength injectate has not been recognised or examined. In this study we analyse and report the mobilisation of fluoride (up to 58 µM) and filterable reactive phosphorus (FRP) (up to 55 µM) during a field groundwater replenishment experiment in which highly treated, deionised wastewater (average TDS 33 mg/L) was injected into a siliciclastic Cretaceous aquifer. In the field experiment, maximum concentrations, which coincided with a rise in pH, exceeded background groundwater concentrations by an average factor of 3.6 for fluoride and 24 for FRP. The combined results from the field experiment, a detailed mineralogical characterisation and geochemical modelling suggested carbonate-rich fluorapatite (CFA: $Ca_{10}(PO_4)_5(CO_3,F)F_2$) to be the most likely source of fluoride and phosphate release. An anoxic batch experiment with powdered CFA-rich nodules sourced from the target aquifer and aqueous solutions of successively decreasing ionic strength closely replicated the field-observed fluoride and phosphate behaviour. Based on the laboratory experiment and geochemical modelling, we hypothesise that the release of fluoride and phosphate results from the incongruent dissolution of CFA and the simultaneous formation of a depleted layer that has hydrated di-basic calcium phosphate ($CaHPO_4 \bullet nH_2O$) composition at the CFA-water interface. Disequilibrium caused by calcium removal following breakthrough of the deionised injectate triggered the release of fluoride and phosphate. Given the increasing use of highly treated, deionised water for MAR and the ubiquitous presence of CFA and fluorapatite ($Ca_{10}(PO_4)_6F_2$) in aquifer settings worldwide, the risk of fluoride and phosphate release needs to be considered in the MAR design process.

**Keywords**: *Managed aquifer recharge, fluoride, phosphate, carbonate-rich fluorapatite, deionised wastewater*

# 1 Introduction

Globally, but especially in arid and semiarid regions, managed aquifer recharge (MAR) is an increasingly used water management tool. It involves infiltration or direct injection of water into suitable aquifers to improve and secure long-term water supplies (Casanova et al., 2016; Dillon and Arshad, 2016). In most applications of MAR, the infiltration or injection of various water types (e.g., surface water, purified wastewater, stormwater runoff) typically creates a geochemical disequilibrium that triggers a wide range of water-rock interactions (Descourvieres et al., 2010a; Fakhreddine et al., 2015; McNab Jr et al., 2009; Treumann et al., 2014; Vanderzalm et al., 2010; Wallis et al., 2011). For selected sedimentary aquifer types, this re-equilibration can induce the risk of mobilising geogenic fluoride (Gaus et al., 2002). While concentrations of fluoride less than 0.5 mg/L (26 µM) in drinking water are considered beneficial to human and animal health, concentrations greater than 1.5 mg/L (79 µM) can lead to dental fluorosis and, in extreme cases, skeletal fluorosis (Edmunds and Smedley, 2013; Fantong et al., 2010; WHO, 2017). While high concentrations of dissolved fluoride are not commonly associated with sedimentary aquifers, elevated fluoride concentrations have been associated with the presence of fluorite ($CaF_2$) in chalk aquifers (Gaus et al., 2002; Malcuit et al., 2014), anion exchange with fluoride-bearing phyllosilicates (Edmunds and Smedley, 2013; Guo et al., 2007), and the biologically and/or chemically derived fluoride-bearing phosphate minerals fluorapatite (FAP: $Ca_{10}(PO_4)_6F_2$) and carbonate-rich fluorapatite (CFA: $Ca_{10}(PO_4)_5(CO_3F)F_2$) (Borgnino et al., 2013; Edmunds and Smedley, 2013; Travi, 1993; Zack, 1980). In weathered and fractured rock aquifers in crystalline terrains, high fluoride concentrations have been commonly associated with the presence of fluorite, as well as primary rock-forming FAP, fluoride-bearing phyllosilicates, and hornblende(Edmunds and Smedley, 2013; Fantong et al., 2010; Rafique et al., 2015; Raju, 2017).

CFA, also referred to as ‘francolite’ in economic deposits, predominantly forms in marine environments under reducing conditions, especially where there is upwelling (Ruttenberg, 2003); Kholodov, 2014). It is, however, also known to form in freshwater lacustrine environments (Föllmi,

1996; Kholodov, 2014). Bone hydroxyapatite ($Ca_{10}(PO_4)_6(OH)_2$) as well as muscle tissue can re-mineralise as CFA (Keenan, 2016). Recent studies have shown that during the Mesozoic, marine and land vertebrates incorporated extensive amounts of FAP into tooth material (enameloid and dentin) whereas, at present, only the enameloid in cartilaginous fish (e.g., sharks) is FAP while all other vertebrate groups have hydroxyapatite tooth material (Lübke et al., 2015). Therefore, the age and depositional history of the sedimentary aquifers may influence the amount of biogenic fluoride-bearing phosphate minerals that are present and whether fluoride may be mobilised during MAR.

CFA is a variety of FAP with a stable defect consisting of a planar carbonate group and fluoride ion pairing that replaces up to approximately 1.4 phosphate tetrahedra per unit cell within the apatite structure (hexagonal *P63/m* space group) (Dorozhkin, 2015; Hughes and Rakovan, 2002; McClellan, 1980; Yi et al., 2013a). Calcium atoms in the FAP structure exist in two different coordinations (9-fold and 7-fold) with oxygen atoms, from the phosphate tetrahedral, and fluoride ions occurring in structural channels (Chaïrat et al., 2007b; Dorozhkin, 2012). Carbonate ions in CFA can also occur in the main structural channels as well as pair with fluoride in phosphate site (Yi et al., 2013a). The apatite structure in general allows a multitude of substitutions (Hughes and Rakovan, 2002; Jarvis et al., 1994; Pan and Fleet, 2002). The substitutions in CFA, especially the main carbonate defect, limit the size to which CFA crystals can grow, usually to 0.3-2 μm in size (McClellan and Lehr, 1969).

The dissolution mechanism of calcium apatite is complex and is still not fully understood (see for example the reviews by Dorozhkin (2002) and Dorozhkin (2012)). CFA and FAP are sparingly soluble under circumneutral pH conditions and have solubility products that vary with pH (Chaïrat et al., 2007a; Jahnke, 1984). Experimental studies have demonstrated that dissolution of CFA and FAP in low ionic strength water and at circumneutral pHs is initially incongruent, whereby the ratios of fluoride to phosphate and calcium to phosphate exceed the stoichiometric ratios existing in the mineral (Bengtsson et al., 2007; Chaïrat et al., 2007b; Guidry and Mackenzie, 2003; Zhu et al., 2009). Based on experiments using FAP, Zhu et al. (2009) found that the preferential release of

phosphate and fluoride accompanied by a rapid rise in solution pH. Dissolution of FAP has been proposed to start as a rapid proton exchange reaction whereby $H^+$ is adsorbed onto the apatite surface triggering the combined released of fluoride and weakly coordinated calcium. This results in the formation of a leached layer of dicalcium phosphate (DCP: $CaHPO_4 \bullet nH_2O$) composition at the FAP surface (Chaïrat et al., 2007a; Christoffersen et al., 1996). Zhu et al. (2009) attributed the observed early preferential release of phosphate to dissolution of crystal edges and corners. Jahnke (1984) also found that during the initial dissolution of synthetic CFA, carbonate ions were also likely to be released preferentially. After the initial incongruent stage, the dissolution of CFA and FAP gradually becomes stoichiometric (Chaïrat et al., 2007b; Guidry and Mackenzie, 2003; Tribble et al., 1995). The stoichiometric dissolution occurs when equilibrium is reached where the rate of release of weakly coordinated calcium, internally from the bulk mineral as $H^+$ ions traverse the leached surface layer, equals the rate of release of more strongly coordinated calcium at the surface layer/solution boundary (Chaïrat et al., 2007b; Tribble et al., 1995). The rate of stoichiometric dissolution of CFA and FAP is relatively slow near and above pH 7 and increases with decreasing pH under acidic conditions (Chaïrat et al., 2007b; Guidry and Mackenzie, 2003).

Aquifers in equilibrium with fluoride-bearing phosphate minerals do not necessarily contain high concentrations of fluoride in groundwater. For example, Travi (1993) noted that groundwater in contact with CFA deposits in north-west Tunisia contained low fluoride concentrations, most likely due to the high dissolved calcium concentrations that persist as a result of the presence of gypsum ($CaSO_4 \bullet 2H_2O$) in the aquifer. However, fluoride mobilisation may occur where dissolved calcium concentrations are low. For example, Travi (1993) noted elevated fluoride concentrations in CFA containing aquifers in Senegal with low calcium concentrations. High fluoride concentrations have also been reported for aquifers containing CFA and trace phosphate minerals where calcium has been removed from groundwater as a result of calcite precipitation (Abu Jabal et al., 2014; Kumar et al., 2018; Rafique et al., 2015) or cation exchange (Edmunds and Smedley, 2013). These naturally occurring water-rock interactions illustrate the potential for fluoride mobilisation to occur during

MAR in cases where the injectate contains lower concentrations of calcium than the native groundwater (NGW).

To our knowledge, the risk of fluoride and phosphate release from aquifers during MAR with low ionic strength water has neither been recognised nor examined. In this study, we report, for the first time, fluoride and phosphate release during a large-scale closely monitored field experiment in which deionised wastewater was injected into a Cretaceous siliclastic aquifer with low background fluoride concentration. Combining field observations with supporting laboratory experiments and geochemical modelling, we identify the trace CFA phases in this aquifer and reveal the mechanisms that control fluoride release.

## 2 Material and Methods

### 2.1 Site characteristics and field injection experiment

A comprehensive field-scale injection experiment was conducted between November 2010 and September 2014 to investigate the feasibility of recharging highly treated wastewater into the Cretaceous siliciclastic Leederville aquifer of the Perth Basin, Western Australia (Figure 1) (Seibert et al., 2016; Seibert et al., 2014). The highly treated wastewater was injected through a single injection well screened between 123.7 and 224.4 m below ground level (bgl) (Figure 2). The targeted injection interval comprised the Wanneroo Member of the Leederville Formation, which is locally confined above by the silty sands, silts, and clays of the Pinjar member and below by both the Mariginiup member and the South Perth Shale (Descourvieres et al., 2011; Leyland, 2011). The Leederville Formation sediments consist of interbedded sand, clay and silt layers that were deposited in a marginal-marine setting (Leyland, 2011). Sand layers are subarkosic and composed mostly of quartz (64%) and K-feldspars (27%), while silt and clay beds contain kaolinite (24–54%), K-feldspar (20–29%) and quartz (18–40%) (Descourvieres et al., 2011). Trace minerals which have been detected include pyrite, lignite, siderite, muscovite and biotite.

Pre-treatment of the wastewater involved ultra-filtration, reverse osmosis and ultra-violet disinfection, resulting in oxic deionised wastewater (Higginson and Martin, 2012). Over the trial period, a total of $3.90 \times 10^6$ $m^3$ of this pre-treated wastewater was injected at an average injection rate of 2800 $m^3$/d. The spreading of the injectant was monitored through an extensive groundwater sampling program through by 20 monitoring wells and time-lapse temperature logging. The 20 monitoring wells were arranged in 5 multilevel well clusters at radial distances of 20, 60, 120, 180 and 240 m from the injection well (Figures 1 and 2). Groundwater quality evolution in all 20 monitoring wells was monitored throughout the trial for a broad range of water quality indicators, including pH, redox potential, dissolved oxygen, alkalinity, major ions, nutrients, heavy metals/metalloids and organic substances. All water quality samples were stored on ice immediately following collection and submitted for analysis the same day. NGW conditions were established at all monitoring wells through repeated groundwater quality sampling commencing approximately 2 years prior to the start of injection. Additionally, injectant samples were taken monthly from the post-treatment reservoir tank shortly before injection and analysed in a similar fashion. Detailed descriptions of the sampling and analytical procedures are given in Water Corporation (2009).

Time lapse temperature and induction logging of the monitoring wells and subsequent solute and heat transport modelling demonstrated that flow and transport occurred preferentially in the interlayered sand beds (Seibert et al., 2014). Previous column experiments and reactive transport modelling identified pyrite oxidation as a key reaction that occurred when the injectant displaced the highly reducing NGW, particularly in the vicinity of the injection well (Descourvieres et al., 2010a; Descourvieres et al., 2010b; Seibert et al., 2016). Acidity generated from pyrite oxidation was found to be buffered by a combination of proton exchange on cation exchange sites and, to a lesser extent, the dissolution of trace carbonate minerals, ankerite and siderite, as well as dissolution of glauconite and chlorite (Seibert et al., 2016). Fluoride and phosphate pulses were observed during breakthrough of the injected pre-treated wastewater.

### 2.2 Characterisation of carbonate-fluorapatite contained in the Leederville Formation sediments

To identify potential sources of fluoride and phosphate, compositional and mineralogical analyses were conducted on the Leederville Formation sediments. From core material collected from a bore ~525 m to the north of the injection well, several apatite-rich nodules were recovered. The interval in which the nodules were found was ~112.2 m bgl within fine grained Leederville Formation sediments. Polished carbon coated sections of these nodules were analysed using a JEOL JSM-7001F emission scanning electron microscope (SEM) with a Bruker Quantax 400 energy dispersive spectroscopy elemental mapping system. High resolution images of the nodule sections were obtained using a Tescan Vega3 and FEI Varios SEM. Compositional analyses of individual micron sized grains within a selected nodule were undertaken using a JEOL JXA-8500F electron microprobe equipped with five wavelength dispersive spectrometers and two energy dispersive spectrometers. The analyses were performed on surfaces polished to a 1 µm diamond finish. The electron probe micro-analyser was operated at an accelerating voltage of 10 kV, beam current of 5 nA and the beam was defocused to 2 µm. The relatively low voltage of 10kV was chosen to reduce the interaction volume as the CFA was fine grained. The suite of elements analysed included Ca, P, F, Al, Cl, S, Fe, Na, and Si. To minimise damage to the sample, and mitigate migration of light elements under the electron beam, counting times were set to 4 seconds for Ca and P, 6 seconds for F, and 10 seconds for the other elements. Standards used were FAP ($\mathbf{Ca}_5(\mathbf{P}O_4)_3\mathbf{F}$), berlinite ($\mathbf{Al}PO_4$), sylvite (K**Cl**), pyrite ($Fe\mathbf{S}_2$), hematite ($\mathbf{Fe}_2O_3$), albite ($\mathbf{Na}AlSi_3O_8$), and wollastonite ($Ca\mathbf{Si}O_3$). All elements analysed were corrected for atomic number, absorption and fluorescence using the CITZAF Phi-Rho-Z correction procedure (Armstrong, 1995) with oxygen calculated by stoichiometry and carbon calculated by difference.

Additionally, the nodules were characterised using both Fourier transform infrared spectroscopy (FTIR) and X-ray diffraction (XRD). FTIR spectra were collected using a Vertex 70 Fourier transform infrared spectrometer and Hyperion 3000 microscope (Bruker). The microscope was

operated in attenuated total reflectance mode using a liquid nitrogen cooled mercury-cadmium-telluride detector. Measurements were made with a 20× objective and an area of 30×30 μm was sampled. Spectra were collected between 4000 to 600 $cm^{-1}$ using 64 scans, a resolution of 2 $cm^{-1}$ and air was used as the background. The FTIR peak assignments are based on various references (Antonakos et al., 2007; Yi et al., 2013b; Zhu et al., 2009). XRD spectra of the nodules were collected using a PANalytical X-Pert Pro XRD system (see Supporting Information for details). The diffraction patterns were matched against the ICDD PDF database using the PANAlytical X'pert Highscore Plus software.

### 2.3 Anoxic batch experiment, sampling and analyses

To investigate whether fluoride and phosphate in the groundwater at the field site were released specifically from CFA, two sets of batch experiments were performed in duplication under anoxic condition that approximately mimicked the geochemical condition during the field injection trial. In the experiment, artificial groundwater in equilibrium with CFA was gradually replaced with artificial deionised injectate (DeI) water, and the solutions were sampled and monitored for compositional changes.

Artificial stock solutions representative of the NGW and the DeI were prepared using analytical grade reagents and ultrapure water. The compositions of the NGW and DeI stock solutions were based on the groundwater composition at the base of the injection interval and the average pre-treated wastewater composition, respectively (Table 1) (Higginson and Martin, 2012). The NGW solution consisted of 426 mg/L $Na^+$, 73 mg/L $HCO_3^-$, 47 mg/L $SO_4^{2-}$ and 580 mg/L $Cl^-$ (ionic strength (I) = 17.35 mM), while the DeI solution consisted of 12.1 mg/L $Na^+$, 17.6 mg/L $HCO_3^-$ and 8.7 mg/L $Cl^-$ (I = 0.53 mM). Five solution mixtures were then made by mixing the stock solutions by volume, as 100% NGW, 75% NGW – 25% DeI, 50% NGW – 50% DeI, 25% NGW – 75% DeI and 100% DeI. All solutions were de-oxygenated by purging with nitrogen gas ($N_2$) before use.

A large CFA rich nodule was collected from the same interval from which the nodule used for the microprobe compositional analysis was sourced. This nodule was ground into a fine powder using an agate mortar. A portion of the powder was analysed for elemental composition by X-ray fluorescence (XRF) with a PANalytical Axios Advanced wavelength dispersive system (see Supporting Information for details). The remainder of the powder was used for the batch experiments.

Two CFA powder samples, sample 1 weighing 0.989 g and sample 2 weighing 0.962 g, were placed in two 15 mL polypropylene centrifuge vials, to each of which 10 mL of the 100% NGW solution was added. The pH was measured using a TPS 90FL-MV multi-parameter instrument with an intermediate junction pH electrode (IJ-44C, Ionode). To remove the acidity generated by pyrite oxidation during exposure of the nodule to air , the pH was adjusted from around pH 4 using NaOH to a pH similar to the NGW, vial 1 pH 7.09 and vial 2 pH 7.23. The pH-adjusted solid-solution mixtures were purged with $N_2$ for 30 minutes. The vials were centrifuged at 3316g for 10 minutes, before the supernatant was decanted and replaced with 10 mL of de-oxygenated 100% NGW solution. The head space in the vials were replaced with $N_2$, capped and transferred to an anoxic chamber (Coy Laboratory Products) where the solid-solution mixtures were equilibrated for 124 days. During the 124 day equilibration period, the mixtures were periodically shaken by hand. After 124 days, the pH of the solid-solution mixtures was measured in the anoxic chamber. The sealed vials were removed from the chamber, centrifuged for 10 minutes at 3316 g, and then transferred back to the chamber. The supernatant was decanted and filtered to 0.45 µm (cellulose acetate membrane, Whatman Puradisc FP 30), and the solids were then treated with 10 mL of de-oxygenated 75% NGW – 25% DeI solution. The capped vials were removed from the chamber and placed on an end-over-end mixer for 60 minutes, before being centrifuged at 3316 g for 10 minutes. The vials were then returned to the chamber where the pH was measured, and the supernatant was decanted and filtered (0.45 µm). This procedure was repeated three times for the remaining mixtures in order of decreasing NGW fraction.

The solution samples were analysed for $Ca^{2+}$, $Mg^{2+}$, $Na^{+}$, $K^{+}$, $Cl^{-}$, $SO_4^{2-}$, $F^{-}$ and $PO_4^{3-}$ concentrations using a Dionex ICS-3000 ion chromatography system. Cations were analysed using IonPac CS16 analytical and guard columns, with an eluent of 30 mM methanesulfonic acid, at a flow rate of 1.2 mL/min. Anions were analysed using IonPac AS18 analytical and guard columns, in gradient mode with eluent concentrations increasing from 12 to 45 mM potassium hydroxide, at a flow rate of 1.0 mL/min. The $F^{-}$ and $PO_4^{3-}$ concentrations were determined using the method of standard additions. Ultrapure water (Milli-Q) was used to prepare standards and dilute samples. Instrument drift was corrected for by the addition of an internal standard (lithium fluoride, 20 mg/L) for determination of ions except for $F^{-}$ and $PO_4^{3-}$. Bicarbonate ($HCO_3^{-}$) was measured separately by titration using a Hanna HI 3811 total alkalinity kit. The NGW – DeI solution mixtures were used in these analyses as blanks.

### 2.4 Geochemical modelling of pre-injection native groundwater and anoxic batch experiment

Saturation indices (SIs) for a suite of potentially labile fluoride and phosphate bearing phases were calculated with PHREEQC (Parkhurst, 2015) under pre-injection native conditions. The standard *Phreeqc.dat* database was modified to include additional fluoride and phosphate minerals and calcium-phosphate salts as well as revised equilibrium constants from the literature. SIs were calculated at 25ºC, consistent with the NGW temperature of 25.3 ± 0.8ºC (n = 88). In total, 88 groundwater compositions from 20 monitoring wells were analysed.

Geochemical modelling of the anoxic batch experiment was undertaken with PHREEQC to test the proposed conceptual model of the processes controlling fluoride and phosphate release with decreasing ionic strength. In the reaction network, CFA dissolution was modelled as an exchange reaction in which CFA dissolution and the formation of hydrated di-basic calcium phosphate (DCP: $CaHPO_4 \bullet nH_2O$) at the water-mineral interface occur simultaneously in response to proton attack,

i.e., changes in pH. The anoxic batch experiment was modelled as a sequence of mixing events and the corresponding adjustments of the water-sediment equilibria:

- The initial exchanger composition prior to the mixing/dilution events was determined through equilibration with the solution composition that was determined after the initial 124 day equilibration period with 100% NGW.
- Decanting and replacing the solution with the 75% NGW – 25% DeI mixture was modelled by mixing the NGW–DeI solutions (~95% of the total volume) with the residual porewater (~5% of the total volume) while maintaining equilibrium with the exchange sites and selected minerals.
- The above step was repeated for 50% NGW – 50% DeI, 25% NGW – 75% DeI, and 100% DeI.

# 3 Results

## 3.1 Pre-injection native groundwater

The NGW in the Leederville aquifer consisted of Na-Cl to Na-Cl-$HCO_3$ type water with a TDS that increased with depth ranging from 400 to 1100 mg/L and low fluoride and phosphorus concentrations of both < 0.3 mg/L (Table 1). The SIs calculated for the pre-injection native conditions indicated that the groundwater was under-saturated with respect to all fluoride and phosphate bearing mineral phases (Figure 3). Among the fluoride and phosphate bearing minerals investigated, the surface layer that has a DCP composition at the FAP-water interface (hereinafter referred to as DCP-surface) (Chaïrat et al., 2007a) was the phase that was closest to equilibrium with the NGW (median SI = -1.07, range -1.42 to +0.18). The groundwater showed to be more under-saturated with respect to the FAP bulk mineral (median SI = -1.69, range -4.16 to +2.54) than with respect to the DCP-surface. This may be indicative of the presence of FAP or CFA at the study site. The SI for CFA was calculated using the solubility product for CFA with a composition of one carbonate ion per unit cell content (Jahnke, 1984). However, Jahnke (1984) showed that the solubility product varies significantly with carbonate content. Since the composition of CFA was not

known *a priori*, it was not possible to determine how close the bulk mineral of CFA is to equilibrium. A number of groundwater samples show SIs near zero for vivianite ($Fe_3(PO_4)_2 \cdot 8H_2O$) (median SI = -2.60, range -4.15 to +0.40), suggesting that this iron phosphate mineral might locally prevail within the aquifer. Fluorite, the presence of which is a common cause of elevated fluoride concentration in groundwater, was always under-saturated (median SI = -3.26, range -4.32 to -2.70) and is presumably absent. The median SI for the carbonate mineral siderite ($FeCO_3$) was +0.09 (range -0.59 to +0.39) and therefore close to saturation. This is consistent with its previous detection in fine-grained Leederville Formation sediments (Descourvieres et al., 2011). A number of other carbonate minerals were under-saturated (calcite median SI = -1.58, dolomite median SI = -2.88, ankerite median SI = -3.12) along with gypsum (median SI = -3.01), as discussed in more detail in Seibert et al. (2016).

### 3.2 Fluoride and phosphate breakthrough behaviour during the field experiment

During the field injection experiment, highly treated wastewater was injected. The pre-treatment resulted in deionised water with low dissolved solids concentration (TDS) of 33.2 ± 10.9 mg/L and relatively high dissolved oxygen concentration of 8.3 ± 0.5 mg/L (Table 1) (Higginson and Martin, 2012). Arrival times of the injectate, as indicated by the decrease in the concentration of the conservative solute chloride, increased with distance from the injection well and varied with depth (Figures 4 and 5). At 20 m from the injection well, the fastest complete breakthrough of chloride occurred after 21 days (at monitoring well BY11), while at 240 m the fastest complete breakthrough occurred after 1155 days (at monitoring well BY17).

Pulses of increased fluoride and phosphate concentration were observed upon breakthrough of the injectate as indicated by $Cl^-$ at most monitoring locations (Figure 4). Generally, increased fluoride concentrations occurred slightly before increased phosphate concentrations. Observed peak concentrations of fluoride ranged from 12 µM to 58 µM, exceeding background concentrations by a factor of 3.6 ± 1.2 (n = 20). Observed peak concentrations of phosphate (measured as filterable

reactive phosphorus, FRP) ranged from 3.9 μM to 55 μM, exceeding background concentrations by a factor of 24.1 ± 16.2 (n = 20). Concentrations of phosphate were consistently lower than fluoride concentration with the ratio of phosphate to fluoride concentrations being 0.82 ± 0.22 (n = 20). With increasing distance from the injection well, the observed pulses of fluoride and phosphate generally became broader while also increasing in amplitude (Figures 4 and 5). A few selected monitoring bores located at 20 m from the injection well (e.g., BY11, BY08 and BY06) showed a small sustained increase in fluoride, while the phosphate pulse declined rapidly (Figure 4). With continued injection, fluoride and phosphate decreased to background concentrations, with the phosphate concentrations declining faster than the fluoride concentrations.

A rise in pH from around 0.2 to 1.0 pH units also occurred upon breakthrough of the DeI (Figures 4 and 5). The rise in pH in proximal bores, i.e., where breakthrough was fast, was generally followed by a slow decrease in pH. More distal bores, on the other hand, show a sustained, elevated pH post breakthrough (Figure 4). During the period when elevated fluoride (0.020 – 0.058 mM) occurred, the pH ranged from 6.6 to 7.7 for all monitoring bores (7.12 ± 0.21, n = 240). During the period when elevated fluoride and phosphate concentrations occurred, dissolved calcium concentrations were low or decreasing while sodium concentrations increased (Figures 5j, 5k). Therefore, Na/Ca ratios were elevated relative to the native ratios that prevailed prior to injection. Synchronous with the decrease in fluoride and phosphate concentrations, the Na/Ca ratios declined to approximately stable values that, however, were lower than the native ratios (Figures 5g – 5i). An increase in bicarbonate concentrations relative to chloride also occurred upon the breakthrough of the DeI during the field experiment (Figures 5d – 5f). The SIs for DCP-surface showed close to equilibrium conditions throughout the experiment (Figures 5m, 5o). The SIs for FAP, on the other hand, indicate a temporary oversaturation while fluoride and phosphate concentrations were elevated. The SIs for FAP and DCP-surface decreased post breakthrough while fluoride and phosphate concentrations declined (Figures 5m, 5n). FAP precipitation during the period of FAP oversaturation was presumably insignificant due to slow kinetics and nucleation considerations (Cappellen and Berner,

1991). The SIs for many other fluoride and phosphate bearing minerals, calcium-phosphate salts and carbonate minerals suggest under-saturation, except for some isolated values for vivianite, β-tricalcium phosphate (β-TCP) and hydroxyapatite during the occurrence of phosphate peak concentrations and for gypsum during the initial stages of breakthrough of the DeI (Figure S3).

### 3.3 Habit and composition of the apatite-rich nodules

Descourvieres et al. (2011) showed that total phosphorus concentration in the aquifer sediments over the injection interval ranged between 0.01 and 0.29 wt% $P_2O_5$ (0.047 ± 0.049 wt%, n = 40). This suggested that phosphate minerals are only present in trace amounts and that consequently it would be difficult to find individual mineral grains from sediment samples (see Pe-Piper and Dolansky (2005)). However, several dark, micaceous, fine grained (~0.3 to 3 cm), apatite-rich nodules were recovered within fine grained Leederville Formation sediments. The SEM images showed that apatite occurs as aggregates of micron-sized crystallites that form an infilling cement between grains of other minerals such as quartz, K-feldspar and kaolinite (Figure 6). This is consistent with the habit and crystal size of CFA (McClellan and Lehr, 1969). Pyrite and carbon clasts commonly occur in association with the apatite cement. The assemblage of minerals associated with CFA is suggestive of a biogenic origin for CFA, from the remineralisation of bone and tissue in an anoxic environment (Kholodov, 2014). High concentrations of barium (443 mg/kg) and strontium (345 mg/kg) found in the CFA nodule (Table S1), which substitute for calcium in the apatite structure (Pan and Fleet, 2002) and are known to concentrate in bones (Trueman and Tuross, 2002), also suggest a biogenic origin.

Compositional analysis of selected apatite crystallites using electron microprobe show a compositional variation between crystallites (Table 2). The $CO_3$ was initially calculated based on the formula $(Ca, Fe, Al, Na)_{10}(PO_4)_{6-x}(CO_3, F)_x(F, OH)_2$, with x depending on the amount of phosphate. The $OH^-$ was then calculated to balance F. All elements were iteratively matrix corrected with the PAP matrix correction algorithm implemented in STRATA (Pouchou, 1993). A representative unit

cell formula for CFA from the Leederville Formation sediments based on the 'francolite' model of McClellan (1980) was found to be $Ca_{9.75}Na_{0.25}(PO_4)_{5.37}(CO_3, F)_{0.55}F_{1.82}(OH)_{0.18}$. It was assumed that trace S, Fe Al and Si present was due to trace pyrite and kaolinite present within the 2 µm microprobe beam size, because the ratios of these elements were consistent with these minerals. The determined composition has a relatively low carbonate content, but is within the range of CFA compositions typically reported from around the world (Guidry and Mackenzie, 2003).

Infrared spectra collected on a selected CFA rich nodule revealed a number of intense IR absorption bands at ~3333, ~1609, 1460-1400, and 1100-950 $cm^{-1}$ (Figure S1). These four bands are characteristic of hydroxyl (OH stretching vibration), water (OH bending vibration), carbonate ($CO_3^{2-}$ stretching vibration), and phosphate ($PO_4^{3-}$ stretching vibration) species, respectively. The OH peak at 3333 $cm^{-1}$ was relatively broad and is typical of a hydroxyl group that has formed hydrogen bonds (H-bonds). Some weak bands were observed in the IR spectra between 3700-3600 $cm^{-1}$, which can be attributed to hydroxyl groups that are not involved in H-bonds or surface OH groups and may also arise from a minor amount of kaolinite that was present. Compared to previous FTIR studies on fluorapatite (Antonakos et al., 2007; Yi et al., 2013b), the OH bending vibration at ~1609 $cm^{-1}$ was much more intense, suggesting that the CFA form our study site has a higher degree of hydration.

### 3.4 Anoxic batch experiment

The phosphorus content of the powdered nodule used in the anoxic batch experiment was found to be 8.73 wt% $P_2O_5$ as determined by XRF. If assuming that all the phosphorus is present as CFA, then 24.4% by weight of the nodule is CFA. Other minerals present in the CFA-rich nodule include quartz, K-feldspar, pyrite, kaolin, chlorite and gypsum as identified by XRD (Figure S2).

The CFA rich powder was equilibrated with the NGW solution for 124 days, after which the dissolved concentrations of fluoride and phosphate were below the detection limits, i.e., below 3 µM in the case of fluoride and 2 µM in the case of phosphate (Table 3 and Figure 7). The dissolved

calcium concentrations, however, were very high with the average concentration being 1.4 mM. Given that no calcium was present in the artificial NGW solution, the elevated calcium concentrations may have been caused by the presence of secondary gypsum ($CaSO_4 \bullet 2H_2O$) in the nodule and cation exchange. The high calcium concentrations suppressed CFA dissolution and resulted in very low fluoride and phosphate concentrations in the NGW solution.

However, fluoride, and subsequently phosphate, were released when the CFA rich powder was brought in contact with successively increasing proportions of DeI (Figure 7a). When the 75% NGW – 25% DeI mixture was added, dissolved fluoride concentration increased to 7 µM. Concentrations increased further to 20.5 µM in the 50% NGW – 50% DeI mixture, and reached a maximum of 45 µM in the 100% DeI solution. In contrast, dissolved phosphate concentrations remained low until contact with the 100% DeI solution, where it reached 27 µM. The pH increased with each successive mixture, from pH 5.8 after the initial 124 day equilibration period to pH 7.4 in the 100% DeI mixture, with the latter being similar to the pH observed during the field trial (Figure 7b). Bicarbonate concentrations also rose during the later stages of the anoxic batch experiment (Figure 7b). Calcium concentrations decreased rapidly after the first mixing step, followed by a gradual decline (Figure 7c). Sodium and chloride concentrations decreased approximately linearly. The SIs for the DCP-surface indicated close to equilibrium conditions (Figure 7c).

### 3.5 Modelling of the anoxic batch experiment

The geochemical mixing and reaction model for the anoxic batch experiment closely replicated the experimental data (Figure 7). Most notably, the modelling results replicate the observed successive increases in fluoride and phosphate concentrations in response to the sequentially decreased ionic strength. To obtain a good agreement between the simulated and observed fluoride and phosphate concentrations, it was important that the simulated pH closely matched the observed pH. The pH was well matched when a proton exchange reaction was included in the model, which agrees well with the previous study of Seibert et al. (2016), who suggested that proton buffering was the main

buffering mechanism at the study site. The best match between simulations and observations was obtained when a cation exchange capacity of 75 mmol/L was used. Including exchange sites in the simulations was also essential to replicate the observed calcium concentrations (Figure 7c).

# 4 Discussion

## 4.1 Conceptual model for fluoride and phosphate release during MAR

Overall the results of the SI calculations for the NGW, the anoxic batch experiment and geochemical modelling of the experiment jointly indicate that CFA with a DCP-surface is the most likely fluoride and phosphate bearing mineral in the studied aquifer. While CFA is the most likely source of phosphate and fluoride, the molar ratio of dissolved phosphate to fluoride that was observed during the field injection experiment (0.82 ± 0.22, n = 20) and also in the anoxic batch experiment (0.59 ± 0.12, n = 2) were inconsistent with a simple stoichiometric dissolution of CFA. Stoichiometric dissolution would have led to a higher phosphate to fluoride ratio, i.e., ~2.1 for the estimated CFA composition.

We therefore hypothesise that incongruous dissolution of CFA occurred, initiated by a proton attack that released calcium and fluoride and therefore resulted in a Ca/F depleted layer on the CFA surface that has a DCP composition, similar to the mechanism proposed by Chaïrat et al. (2007b). The observed pH during the period of fluoride and phosphate release (range between 6.6 and 7.7, Figures 4, 5 and 7) is always below pH 8.4, the point of zero charge of CFA from the literature (Perrone et al., 2002), and consistent with proton attack being the main dissolution mechanism. For the estimated CFA composition, the initial rapid proton exchange reaction that forms a depleted layer that has DCP composition can be described as:

$$\equiv Ca_{9.75}Na_{0.25}(PO_4)_{5.37}(CO_3,F)_{0.55}F_{1.82}(OH)_{0.18} + 5.37H^+ + nH_2O \leftrightarrow \equiv Ca_{5.37}H_{5.37}(PO_4)_{5.37} \cdot nH_2O + 4.38Ca^{2+} + 0.25Na^+ + 0.55{CO_3}^{2-} + 2.37F^- + 0.18OH^- \quad (1)$$

In conjunction with the rapid exchange reaction, dissolved Ca and phosphate concentrations are also affected by equilibrium with the DCP surface (Chaïrat et al., 2007b; Guidry and Mackenzie, 2003):

$$\equiv Ca_{5.37}H_{5.37}(PO_4)_{5.37} \cdot nH_2O \leftrightarrow 5.37Ca^{2+} + 5.37HPO_4{}^{2-} + nH_2O \quad (2)$$

Contact between CFA-rich sediments and low ionic strength water results in the dissolution of CFA and subsequently the release of calcium, fluoride, and phosphate as well as bicarbonate. Fluoride and phosphate are not released according to the stoichiometric ratio because phosphate is also involved in the equilibrium reactions with the depleted DCP surface that controls the apparent solubility of CFA (Chaïrat et al. (2007a); Zhu et al. (2009)).

The recession of fluoride and phosphate release coincided with an increase in the groundwater calcium concentrations, which appears to have prevented any further dissolution of CFA (Figures 5j – 5k). Low concentrations of calcium observed during the period of elevated fluoride and phosphate concentration most likely resulted from a number of mechanisms, including (i) mostly cation exchange reactions resulting from the compositional change induced by the injectate and (ii) although to a lesser degree, the formation of the DCP surface and sorption. To gain further mechanistic insights into the reactive processes, various calcium and sodium ratios are plotted for BY13 (Figure 8). The initial Na/Ca ratio was 23.10 ± 1.05 (n = 15) at equilibrium under NGW conditions (Figure 8c). After breakthrough of the DeI, the Na/Ca ratio initially increased to > 100. These values (apart from an initial single anomalously high value) were, however, lower than the ratio in the DeI, which was > 180 (Table 1). The Na/Ca ratio then decreased with the receding fluoride and phosphate pulses, before attaining a new, lower equilibrium value of 17.0 ± 0.78 (n = 8) under the then prevailing lower ionic strength conditions (Figures 8a, 8c). The general trend of post-breakthrough, decreasing Na/Ca ratios is consistent with a net sodium exchange for calcium on the exchange sites. The exchangeable sodium ratio, ESR = [Na] / ([Ca] + [Mg])$^{0.5}$, where square brackets represent activities (Appelo and Postma, 2005), shows stable values under NGW conditions (8.65 ± 0.33, n = 15) (Figure 8d). ESR values decreased during the period of elevated fluoride and phosphate concentrations before stabilising at a new equilibrium value (1.79 ± 0.04, n = 8) after fluoride and phosphate concentrations have receded (Figures 8a, 8d). The trend of decreasing ESR is consistent with a net increase of divalent calcium and magnesium on the exchange sites during the

shift to low ionic strength conditions. This general behaviour is replicated by the geochemical model that relied on two key processes, ion exchange and dissolution of CFA. Due to the poor mineral buffering capacity and the low reactivity of the sediments, the overall hydrochemical evolution, including pH, was strongly affected by ion exchange. The prevailing pH then influenced the rate of CFA dissolution while the prevailing Ca concentration controlled the dissolved phosphate concentrations.

### 4.2 Anticipated long-term behaviour

During the investigated field experiment the elevated fluoride and phosphate concentrations showed to be temporary and fluoride did not exceed the WHO drinking water guideline value of 1.5 mg/L (79 µM) (Figure 4). With a continued injection, the pulses of elevated fluoride and phosphate will migrate further into the aquifer along the edge of the radially growing injection plume of deionised wastewater, i.e., the locations where low calcium concentrations persist. In the absence of any attenuation reaction, the fluoride and phosphate pulses at the injectate plume front would be expected to grow with continued injection. However, increased mixing and dispersion as well as adsorption onto kaolinite (Cochiara and Phillips, 2008; Edzwald et al., 1976) and iron and aluminium oxides (Goldberg and Sposito, 1984) are likely to attenuate fluoride and phosphate concentrations.

## 5 Conclusions

This study investigated the processes controlling the fate of fluoride and phosphate during groundwater replenishment of a Cretaceous siliciclastic deep aquifer with recycled, highly treated wastewater. Trace CFA was found to be the most likely source of the temporarily elevated fluoride and phosphate concentrations during the field injection experiment. Complementary anoxic batch experiments with powdered CFA rich nodules sourced from the target aquifer reproduced the field-observed fluoride and phosphate behaviour when high ionic strength water was successively

displaced by low ionic strength water. The identified conceptual model for phosphate and fluoride release that was derived from the field and laboratory investigations involves the following steps:

- DeI successively displaces NGW near the injection well.
- During breakthrough of the injectate, a strong decrease in calcium concentrations that resulted from the combination of groundwater compositional change and cation exchange favoured the transient release of fluoride and phosphate from CFA.
- Phosphate concentrations remained controlled by equilibrium with a depleted layer of dicalcium phosphate composition at the CFA-water interface.
- A rebound of groundwater Ca concentrations from exchange sites prevented the further dissolution of CFA, which resulted in a steady decline of fluoride and phosphate concentrations.

While groundwater fluoride and phosphate concentrations receded at all locations that were monitored during the injection experiment, in a full-scale replenishment scheme, the pulses of elevated fluoride and phosphate concentrations may keep growing radially with continued injection, co-located with the injection plume front. However, the release will be ultimately balanced by adsorption onto sediment surfaces such as the positive edges of kaolinite and amorphous iron and aluminium oxides.

Chemically and/or biologically derived CFA and FAP are ubiquitous in aquifers settings worldwide, especially in marine and Mesozoic sediments. During MAR with low ionic strength water in such settings, the potential for the release of fluoride and phosphate needs to be carefully considered. The mechanism of fluoride and phosphate release due to incongruous dissolution of CFA where disequilibrium caused by calcium removal triggers anomalously high fluoride and phosphate concentrations may also be relevant in many sedimentary aquifers containing CFA or FAP. Furthermore, in the absence of other sources, dissolution of primary rock-forming FAP mediated by

low calcium concentration may also explain high fluoride concentrations (> 1 mg/L) in weathered and fractured rock aquifers in crystalline terrains.

## Acknowledgements

We gratefully acknowledge the financial support for DS through a Robert and Maude Gledden scholarship through the University of Western Australia and topup scholarships by the National Centre for Groundwater Research and Training (NCGRT) and CSIRO Land and Water. We also thank Andrew Rate and Joanne Vanderzalm for their comments on earlier versions of this manuscript.

## References


Abu Jabal, M.S., Abustan, I., Rozaimy, M.R., Al-Najar, H., 2014. Fluoride enrichment in groundwater of semi-arid urban area: Khan Younis City, southern Gaza Strip (Palestine). Journal of African Earth Sciences, 100(0): 259-266. DOI:http://dx.doi.org/10.1016/j.jafrearsci.2014.07.002

Al-Borno, A., Tomson, M.B., 1994. The temperature dependence of the solubility product constant of vivianite. Geochimica et Cosmochimica Acta, 58(24): 5373-5378. DOI:http://dx.doi.org/10.1016/0016-7037(94)90236-4

Al, T.A., Martin, C.J., Blowes, D.W., 2000. Carbonate-mineral/water interactions in sulfide-rich mine tailings. Geochimica et Cosmochimica Acta, 64(23): 3933-3948. DOI:http://dx.doi.org/10.1016/S0016-7037(00)00483-X

Antonakos, A., Liarokapis, E., Leventouri, T., 2007. Micro-Raman and FTIR studies of synthetic and natural apatites. Biomaterials, 28(19): 3043-3054. DOI:https://doi.org/10.1016/j.biomaterials.2007.02.028

Appelo, C.A.J., Postma, D., 2005. Geochemistry, groundwater and pollution. A.A. Balkema, 649 pp.

Armstrong, J.T., 1995. CITZAF: A Package of Correction Programs for the Quantitative Electron Microbeam X-ray Analysis of Thick Polished Materials, Thin Films, and Particles. Microbeam analysis, 4: 4.

Banerjee, A., 2015. Groundwater fluoride contamination: A reappraisal. Geoscience Frontiers, 6(2): 277-284. DOI:http://dx.doi.org/10.1016/j.gsf.2014.03.003

Bengtsson, Å., Lindegren, M., Sjöberg, S., Persson, P., 2007. Dissolution, adsorption and phase transformation in the fluorapatite–goethite system. Applied Geochemistry, 22(9): 2016-2028. DOI:http://dx.doi.org/10.1016/j.apgeochem.2007.05.001

Blanc, P., 2015. Thermoddem - Thermochemical and Mineralogical Tables for Geochemical Modeling. In: Minières), B.B.d.R.G.e. (Ed.), Orléans, France.

Borgnino, L. et al., 2013. Mechanisms of fluoride release in sediments of Argentina's central region. Science of The Total Environment, 443(0): 245-255. DOI:http://dx.doi.org/10.1016/j.scitotenv.2012.10.093

Cappellen, P.V., Berner, R.A., 1991. Fluorapatite crystal growth from modified seawater solutions. Geochimica et Cosmochimica Acta, 55(5): 1219-1234. DOI:http://dx.doi.org/10.1016/0016-7037(91)90302-L

Casanova, J., Devau, N., Pettenati, M., 2016. Managed Aquifer Recharge: An Overview of Issues and Options. In: Jakeman, A.J., Barreteau, O., Hunt, R.J., Rinaudo, J.-D., Ross, A. (Eds.), Integrated Groundwater Management: Concepts, Approaches and Challenges. Springer International Publishing, Cham, pp. 413-434. DOI:10.1007/978-3-319-23576-9_16

Chaïrat, C., Oelkers, E.H., Schott, J., Lartigue, J.-E., 2007a. Fluorapatite surface composition in aqueous solution deduced from potentiometric, electrokinetic, and solubility measurements, and spectroscopic observations. Geochimica et Cosmochimica Acta, 71(24): 5888-5900. DOI:http://dx.doi.org/10.1016/j.gca.2007.09.026

Chaïrat, C., Schott, J., Oelkers, E.H., Lartigue, J.-E., Harouiya, N., 2007b. Kinetics and mechanism of natural fluorapatite dissolution at 25°C and pH from 3 to 12. Geochimica et Cosmochimica Acta, 71(24): 5901-5912. DOI:http://dx.doi.org/10.1016/j.gca.2007.08.031

Cochiara, S.G., Phillips, B.L., 2008. NMR spectroscopy of naturally occurring surface-adsorbed fluoride on Georgia kaolinite. Clays and Clay Minerals, 56(1): 90-99. DOI:10.1346/ccmn.2008.0560108

Descourvieres, C., Douglas, G., Leyland, L., Hartog, N., Prommer, H., 2011. Geochemical reconstruction of the provenance, weathering and deposition of detrital-dominated sediments in the Perth Basin: The Cretaceous Leederville Formation, south-west Australia. Sedimentary Geology, 236(1–2): 62-76. DOI:http://dx.doi.org/10.1016/j.sedgeo.2010.12.006

Descourvieres, C., Hartog, N., Patterson, B.M., Oldham, C., Prommer, H., 2010a. Geochemical controls on sediment reactivity and buffering processes in a heterogeneous aquifer. Applied Geochemistry, 25(2): 261-275. DOI:http://dx.doi.org/10.1016/j.apgeochem.2009.11.012

Descourvieres, C., Prommer, H., Oldham, C., Greskowiak, J., Hartog, N., 2010b. Kinetic Reaction Modeling Framework for Identifying and Quantifying Reductant Reactivity in Heterogeneous Aquifer Sediments. Environmental Science & Technology, 44(17): 6698-6705. DOI:10.1021/es101661u

Dillon, P., Arshad, M., 2016. Managed Aquifer Recharge in Integrated Water Resource Management. In: Jakeman, A.J., Barreteau, O., Hunt, R.J., Rinaudo, J.-D., Ross, A. (Eds.), Integrated Groundwater

Management: Concepts, Approaches and Challenges. Springer International Publishing, Cham, pp. 435-452. DOI:10.1007/978-3-319-23576-9_17

Dorozhkin, S.V., 2002. A review on the dissolution models of calcium apatites. Progress in Crystal Growth and Characterization of Materials, 44(1): 45-61. DOI:http://dx.doi.org/10.1016/S0960-8974(02)00004-9

Dorozhkin, S.V., 2012. Dissolution mechanism of calcium apatites in acids: A review of literature. World journal of methodology, 2(1): 17.

Dorozhkin, S.V., 2015. Calcium orthophosphate deposits: Preparation, properties and biomedical applications. Materials Science and Engineering: C, 55: 272-326. DOI:http://dx.doi.org/10.1016/j.msec.2015.05.033

Edmunds, W.M., Smedley, P., 2013. Fluoride in Natural Waters. In: Selinus, O. (Ed.), Essentials of Medical Geology. Springer Netherlands, pp. 311-336. DOI:10.1007/978-94-007-4375-5_13

Edzwald, J.K., Toensing, D.C., Leung, M.C.-Y., 1976. Phosphate adsorption reactions with clay minerals. Environmental Science & Technology, 10(5): 485-490. DOI:10.1021/es60116a001

Fakhreddine, S., Dittmar, J., Phipps, D., Dadakis, J., Fendorf, S., 2015. Geochemical Triggers of Arsenic Mobilization during Managed Aquifer Recharge. Environmental Science & Technology, 49(13): 7802-7809. DOI:10.1021/acs.est.5b01140

Fantong, W.Y. et al., 2010. Geochemical provenance and spatial distribution of fluoride in groundwater of Mayo Tsanaga River Basin, Far North Region, Cameroon: implications for incidence of fluorosis and optimal consumption dose. Environmental Geochemistry and Health, 32(2): 147-163. DOI:10.1007/s10653-009-9271-4

Föllmi, K.B., 1996. The phosphorus cycle, phosphogenesis and marine phosphate-rich deposits. Earth-Science Reviews, 40(1–2): 55-124. DOI:http://dx.doi.org/10.1016/0012-8252(95)00049-6

Gaus, I., Shand, P., Gale, I.N., Williams, A.T., Eastwood, J.C., 2002. Geochemical modelling of fluoride concentration changes during Aquifer Storage and Recovery (ASR) in the Chalk aquifer in Wessex, England. Quarterly Journal of Engineering Geology and Hydrogeology, 35(2): 203-208. DOI:10.1144/1470-9236/2001-52

Goldberg, S., Sposito, G., 1984. A Chemical Model of Phosphate Adsorption by Soils: II. Noncalcareous Soils. Soil Science Society of America Journal, 48(4): 779-783. DOI:10.2136/sssaj1984.03615995004800040016x

Guidry, M.W., Mackenzie, F.T., 2003. Experimental study of igneous and sedimentary apatite dissolution: Control of pH, distance from equilibrium, and temperature on dissolution rates. Geochimica et Cosmochimica Acta, 67(16): 2949-2963. DOI:http://dx.doi.org/10.1016/S0016-7037(03)00265-5

Guo, Q., Wang, Y., Ma, T., Ma, R., 2007. Geochemical processes controlling the elevated fluoride concentrations in groundwaters of the Taiyuan Basin, Northern China. Journal of Geochemical Exploration, 93(1): 1-12. DOI:http://dx.doi.org/10.1016/j.gexplo.2006.07.001

Higginson, S., Martin, M., 2012. Groundwater Replenishment Trial - Groundwater Report - 2012, Water Corporation.

Hughes, J.M., Rakovan, J., 2002. The Crystal Structure of Apatite, Ca5(PO4)3(F,OH,Cl). Reviews in Mineralogy and Geochemistry, 48(1): 1-12. DOI:10.2138/rmg.2002.48.1

Jahnke, R.A., 1984. The synthesis and solubility of carbonate fluorapatite. American Journal of Science, 284(January, 1984): 21.

Jarvis, I. et al., 1994. Phosphorite geochemistry: state-of-the-art and environmental concerns. Eclogae Geologicae Helvetiae, 87: 58.

Keenan, S.W., 2016. From bone to fossil: A review of the diagenesis of bioapatite. The American Mineralogist, 101(9): 1943-1951. DOI:10.2138/am-2016-5737

Kholodov, V.N., 2014. Geochemical problems of the behavior of phosphorus: A basis for the biogenic hypothesis of phosphorite formation. Lithol Miner Resour, 49(3): 228-249. DOI:10.1134/S0024490214030043

Kumar, S., Venkatesh, A.S., Singh, R., Udayabhanu, G., Saha, D., 2018. Geochemical signatures and isotopic systematics constraining dynamics of fluoride contamination in groundwater across Jamui district, Indo-Gangetic alluvial plains, India. Chemosphere, 205: 493-505. DOI:https://doi.org/10.1016/j.chemosphere.2018.04.116

Leyland, L., 2011. Hydrogeology of the Leederville aquifer, Central Perth Basin, Western Australia, University of Western Australia, 164 pp.

Lübke, A. et al., 2015. Dental lessons from past to present: ultrastructure and composition of teeth from plesiosaurs, dinosaurs, extinct and recent sharks. RSC Advances, 5(76): 61612-61622. DOI:10.1039/C5RA11560D

Malcuit, E., Atteia, O., Larroque, F., Franceschi, M., Pryet, A., 2014. On the role of low-permeability beds in the acquisition of F and SO4 concentrations in a multi-layer aquifer, South-West France. Journal of Contaminant Hydrology, 169(0): 37-49. DOI:http://dx.doi.org/10.1016/j.jconhyd.2014.05.001

McClellan, G.H., 1980. Mineralogy of carbonate fluorapatites. Journal of the Geological Society, 137(6): 675-681. DOI:10.1144/gsjgs.137.6.0675

McClellan, G.H., Lehr, J.R., 1969. Crystal chemical investigation of natural apatites. The American Mineralogist, 54(September-October): 18.

McNab Jr, W.W., Singleton, M.J., Moran, J.E., Esser, B.K., 2009. Ion exchange and trace element surface complexation reactions associated with applied recharge of low-TDS water in the San Joaquin Valley, California. Applied Geochemistry, 24(1): 129-137. DOI:http://dx.doi.org/10.1016/j.apgeochem.2008.11.009

Pan, Y., Fleet, M.E., 2002. Compositions of the Apatite-Group Minerals: Substitution Mechanisms and Controlling Factors. Reviews in Mineralogy and Geochemistry, 48(1): 13-49. DOI:10.2138/rmg.2002.48.2

Parkhurst, D.L., 2015. PHREEQC (Version 3)--A Computer Program for Speciation, Batch-Reaction, One-Dimensional Transport, and Inverse Geochemical Calculations. US Geological Survey.

Pe-Piper, G., Dolansky, L.M., 2005. Early diagenetic origin of Al phosphate-sulfate minerals (woodhouseite and crandallite series) in terrestrial sandstones, Nova Scotia, Canada. American Mineralogist, 90(8-9): 1434-1441. DOI:10.2138/am.2005.1790

Perrone, J., Fourest, B., Giffaut, E., 2002. Surface Characterization of Synthetic and Mineral Carbonate Fluoroapatites. Journal of Colloid and Interface Science, 249(2): 441-452. DOI:http://dx.doi.org/10.1006/jcis.2002.8255

Pouchou, J.-L., 1993. X-Ray microanalysis of stratified specimens. Analytica Chimica Acta, 283(1): 81-97. DOI:https://doi.org/10.1016/0003-2670(93)85212-3

Rafique, T. et al., 2015. Geochemical controls of high fluoride groundwater in Umarkot Sub-District, Thar Desert, Pakistan. Science of The Total Environment, 530: 271-278. DOI:http://dx.doi.org/10.1016/j.scitotenv.2015.05.038

Raju, N.J., 2017. Prevalence of fluorosis in the fluoride enriched groundwater in semi-arid parts of eastern India: Geochemistry and health implications. Quaternary International, 443: 265-278. DOI:https://doi.org/10.1016/j.quaint.2016.05.028

Ruttenberg, K.C., 2003. chapter 8.13 The global phosphorus cycle. In: Schlesinger, W.H. (Ed.), Treatise on Geochemistry. Elsevier.

Seibert, S. et al., 2016. Identification and quantification of redox and pH buffering processes in a heterogeneous, low carbonate aquifer during managed aquifer recharge. Water Resources Research, 52(5): 4003-4025. DOI:10.1002/2015WR017802

Seibert, S. et al., 2014. Heat and mass transport during a groundwater replenishment trial in a highly heterogeneous aquifer. Water Resources Research, 50(12): 9463-9483. DOI:10.1002/2013WR015219

Stumm, W., Morgan, J.J., 1996. Aquatic chemistry, chemical equilibria and rates - in natural waters. Wiley-Interscience.

Travi, Y., 1993. Hydrogéologie et hydrochimie des aquifères du Sénégal - Hydrogéochimie du fluor dans les eaux souterraines (Hydrogeology and hydrochemistry of the aquifers of Senegal -Hydrogeochemistry of fluoride in groundwater). Sciences Geologiques, Université Louis Pasteur de Strasbourg, Memoire 95: 155.

Treumann, S., Torkzaban, S., Bradford, S.A., Visalakshan, R.M., Page, D., 2014. An explanation for differences in the process of colloid adsorption in batch and column studies. Journal of Contaminant Hydrology, 164(0): 219-229. DOI:http://dx.doi.org/10.1016/j.jconhyd.2014.06.007

Trueman, C.N., Tuross, N., 2002. Trace Elements in Recent and Fossil Bone Apatite. Reviews in Mineralogy and Geochemistry, 48(1): 489-521. DOI:10.2138/rmg.2002.48.13

Vanderzalm, J.L., Page, D.W., Barry, K.E., Dillon, P.J., 2010. A comparison of the geochemical response to different managed aquifer recharge operations for injection of urban stormwater in a carbonate aquifer. Applied Geochemistry, 25(9): 1350-1360. DOI:http://dx.doi.org/10.1016/j.apgeochem.2010.06.005

Wagman, D.D. et al., 1982. NBS tables of chemical thermodynamic properties. Journal of Physical Chemistry, Chem. Ref. Data 111(Suppl. 1).

Water_Corporation, 2009. Site Characterisation Report - Groundwater Replenishment Trial. Water Corporation, pp. 163.

Wallis, I. et al., 2011. Process-Based Reactive Transport Model To Quantify Arsenic Mobility during Aquifer Storage and Recovery of Potable Water. Environmental Science & Technology, 45(16): 6924-6931. DOI:10.1021/es201286c

WHO, 2017. Guidelines for Drinking-water quality. World Health Organization, pp. 541.

Yi, H. et al., 2013a. A carbonate-fluoride defect model for carbonate-rich fluorapatite. American Mineralogist, 98(5-6): 4.

Yi, H. et al., 2013b. A carbonate-fluoride defect model for carbonate-rich fluorapatite. The American Mineralogist, 98(5-6): 1066-1069. DOI:10.2138/am.2013.4445

Zack, A.L., 1980. Geochemistry of Fluoride in the Black Creek Aquifer System of Horry and Georgetown Counties, South Carolina - and its Physiological Implications. Water-supply paper 2067, USGS.

Zhu, Y. et al., 2009. A comparative study on the dissolution and solubility of hydroxylapatite and fluorapatite at 25°C and 45°C. Chemical Geology, 268(1–2): 89-96. DOI:http://dx.doi.org/10.1016/j.chemgeo.2009.07.014

## Tables

**Table 1**: Average composition for DeI and composition of NGW from selected monitoring wells (Higginson and Martin, 2012).

| | | NGW (representative analyses) | | | DeI |
|---|---|---|---|---|---|
| **Location** | **Site** | **BY04: 120m East** | **BY02: 120m East** | **BY01: 120m East** | |
| **Screen depth** | **m bgl[#]** | **127.5 – 130.5** | **165.3 – 171.3** | **203.3 – 209.3** | |
| **Sample date** | **Date** | **21-Oct-10** | **21-Oct-10** | **21-Oct-10** | **17-Nov-10 to 19-Aug-14** |
| **pH** | - | 6.70 | 6.71 | 6.67 | 7.00 (sd = 0.10, n = 77) |
| **Temperature** | °C | 24.1 | 24.9 | 26.2 | - |
| **Dissolved oxygen** | mg/L | - | - | - | 8.3 (sd = 0.5, n = 78) |
| **TDS** | mg/L | 410 | 870 | 1100 | 33.2 (sd = 10.9, n = 51) |
| **Cl** | mg/L | 168 | 468 | 639 | 7.0 (sd = 2.1, n = 39) |
| **Na** | mg/L | 82.2 | 234 | 355 | 10.3 (sd = 2.4, n = 39) |
| **$HCO_3$** | mg/L | 92 | 73 | 104 | 13.9 (sd = 7.2, n = 39) |
| **$SO_4$** | mg/L | 9.4 | 40.2 | 75 | 0.14 (sd = 0.08, n = 39) |
| **Ca** | mg/L | 26.8 | 23.8 | 21.2 | 0.10 (sd = 0, n = 39) |
| **Si as $SiO_2$** | mg/L | 24 | 30 | 28 | 0.88 (sd = 0.31, n = 39) |
| **K** | mg/L | 9.2 | 15.4 | 16.1 | 1.0 (sd = 0.3, n = 39) |
| **Mg** | mg/L | 8.9 | 25.6 | 30.6 | 0.11 (sd = 0.03, n = 39) |
| **Fe (filtered)** | mg/L | 5.7 | 7.7 | 9.1 | 0.005 (sd = 0, n = 50) |
| **Br** | mg/L | 0.5 | 1.2 | 1.6 | 0.02 (sd = 0, n = 39) |
| **N (total)** | mg/L | 0.25 | 0.23 | 0.21 | 2.50 (sd = 0.82, n = 50) |
| **F** | mg/L | 0.1 | 0.17 | 0.26 | 0.12 (sd = 0.07, n = 39) |
| **FRP*** | mg/L | 0.07 | 0.18 | 0.28 | 0.01 (sd = 0, n = 50) |
| **P (total)** | mg/L | 0.09 | 0.19 | 0.28 | 0.02 (sd = 0.01, n = 50) |
| **B** | mg/L | 0.05 | 0.09 | 0.1 | 0.10 (sd = 0.03, n = 50) |
| **Mn (filtered)** | mg/L | 0.053 | 0.053 | 0.081 | 0.001 (sd = 0, n = 16) |
| **Al (filtered)** | mg/L | 0.006 | 0.008 | 0.011 | 0.005 (sd = 0, n = 16) |

*FRP = Filterable (molybdate) reactive phosphorus [#]meters below ground level

**Table 2**: Compositional analysis of CFA determined using microprobe (refer Figure 6 for location of analysis points).

| Sample Point | Major elements (weight %) | | | | | | | | | | | |
|---|---|---|---|---|---|---|---|---|---|---|---|---|
| | F | P | Ca | Fe | Na | Al | Cl | Si | S | O | C | H |
| 1 | 4.30 | 15.31 | 34.49 | 1.24 | 0.57 | 0.65 | 0.02 | 0.82 | 0.47 | 38.08 | 0.77 | 0.03 |
| 2 | 4.04 | 15.36 | 35.65 | 1.37 | 0.45 | 0.50 | 0.02 | 0.70 | 0.46 | 39.08 | 0.90 | 0.05 |
| 3 | 4.11 | 15.66 | 33.31 | 1.54 | 0.43 | 0.62 | 0.03 | 0.75 | 0.49 | 36.54 | 0.42 | 0.00 |
| 4 | 4.32 | 15.36 | 34.63 | 0.74 | 0.54 | 0.15 | 0.01 | 0.22 | 0.51 | 35.95 | 0.57 | 0.00 |
| 5 | 4.05 | 15.20 | 33.14 | 1.66 | 0.61 | 0.35 | 0.02 | 0.56 | 0.47 | 36.27 | 0.57 | 0.01 |
| 6 | 4.45 | 16.38 | 35.93 | 0.96 | 0.49 | 0.26 | 0.04 | 0.28 | 0.57 | 37.47 | 0.46 | 0.00 |
| 7 | 4.17 | 15.75 | 35.01 | 1.03 | 0.44 | 0.70 | 0.08 | 0.96 | 0.55 | 38.54 | 0.66 | 0.02 |
| mean | 4.21 | 15.57 | 34.59 | 1.22 | 0.50 | 0.46 | 0.03 | 0.61 | 0.50 | 37.42 | 0.62 | 0.02 |
| sd | 0.15 | 0.41 | 1.07 | 0.33 | 0.07 | 0.21 | 0.02 | 0.28 | 0.04 | 1.20 | 0.17 | 0.02 |

**Table 3**: Results from anoxic batch experiment analyses.

| Solution | pH | Na (µM) | Ca (µM) | Mg (µM) | K (µM) | Cl (µM) | $SO_4$ (µM) | alkalinity as $HCO_3$ (µM) | $PO_4$ (µM) | F (µM) |
|---|---|---|---|---|---|---|---|---|---|---|
| 100% NGW1[#] | 5.72 | 17100 | 1840 | 393 | 89 | 18100 | 4479 | 639 | <2 | <3 |
| 100% NGW2[#] | 6.06 | 17300 | 951 | 210 | 73 | 17700 | 2531 | 300 | <2 | <3 |
| 75% NGW – 25% DeI1* | 6.38 | 12900 | 206 | 44 | 35 | 13000 | 624 | 520 | <2 | <3 |
| 75% NGW – 25% DeI2* | 6.46 | 13000 | 154 | 33 | 26 | 12800 | 484 | 669 | <2 | 7 |
| 50% NGW – 50% DeI1* | 6.52 | 8890 | 63 | 13 | 16 | 8810 | 263 | 580 | <2 | 20 |
| 50% NGW – 50% DeI2* | 6.74 | 8860 | 98 | 12 | 15 | 8520 | 236 | 609 | <2 | 21 |
| 25% NGW – 75% DeI1* | 6.84 | 4880 | 93 | 5 | 22 | 4280 | 126 | 659 | 4 | 29 |
| 25% NGW – 75% DeI2* | 6.94 | 5030 | 111 | 5 | 9 | 4360 | 121 | 619 | 5 | 31 |
| 100% DeI1* | 7.38 | 972 | 75 | 2 | 13 | 453 | 13 | 580 | 24 | 46 |
| 100% DeI2* | 7.53 | 970 | 39 | 2 | 3 | 442 | 9 | 500 | 30 | 44 |

[#] 124 days equilibration  * 1 hour mixing

## Figures

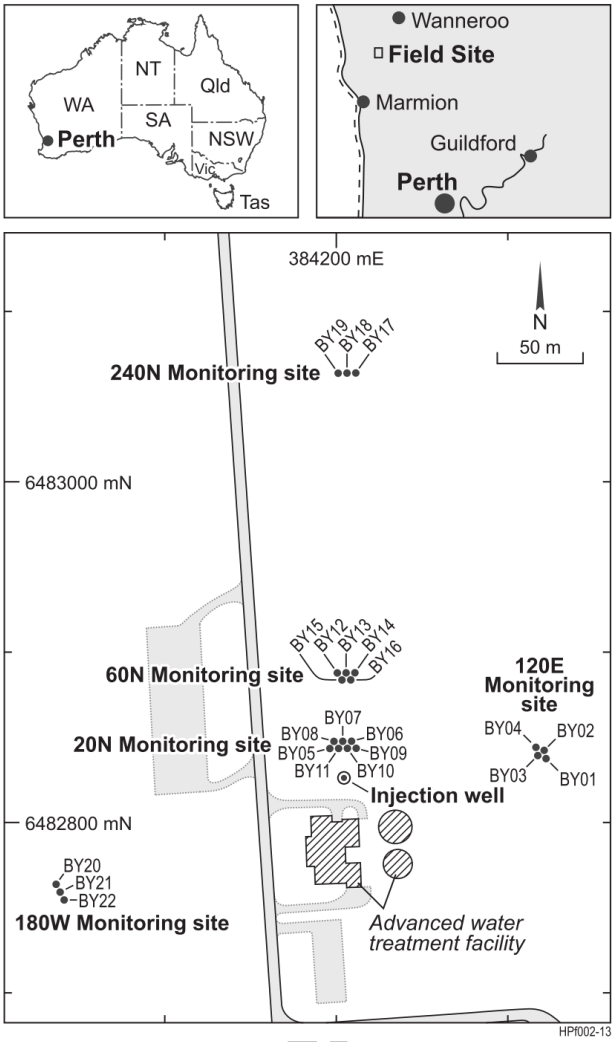


**Figure 1:** Perth groundwater replenishment field injection trial site showing location of injection well, monitoring wells and reverse osmosis water treatment facilities.

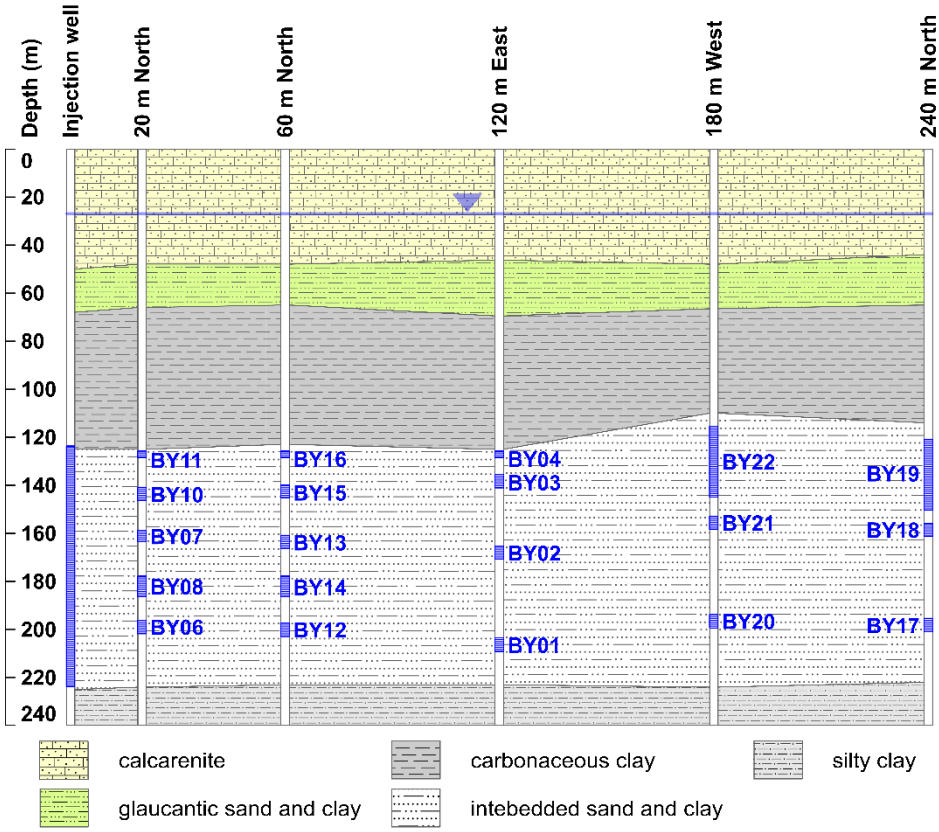


**Figure 2:** Schematic radial cross-section centred on the injection well. All monitoring wells (shown as separate screens intervals at each monitoring location) are projected onto the cross-section.

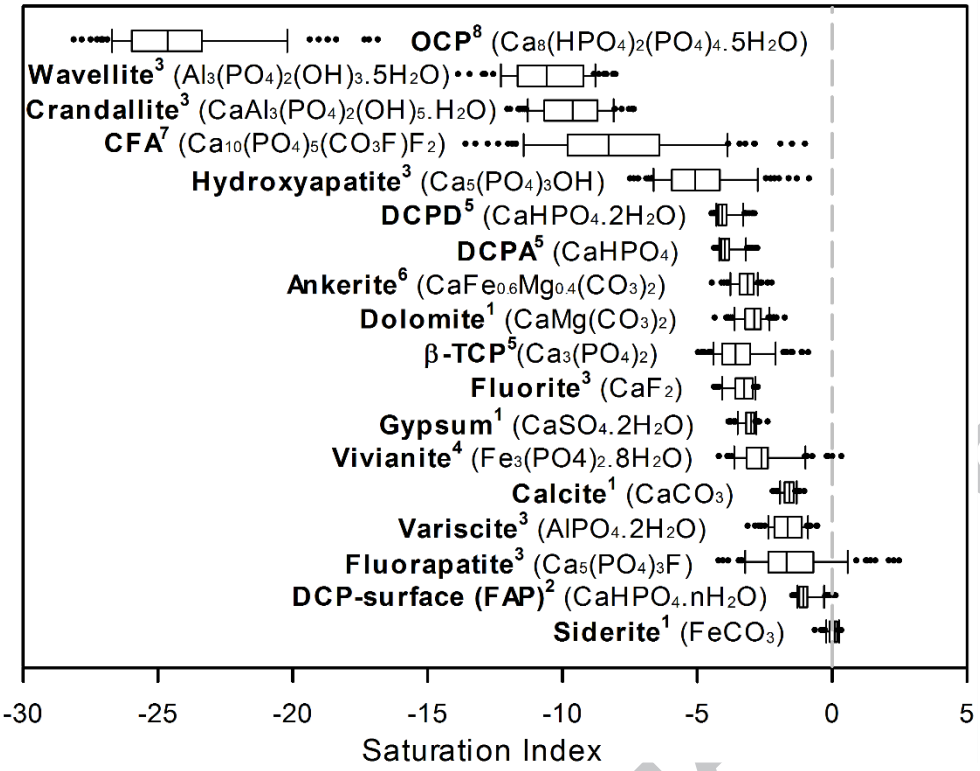


**Figure 3:** Saturation indices for potential fluoride and phosphate bearing phases, carbonate minerals and gypsum for 88 samples from 20 monitoring wells prior to the start of injection. The line within the box is the median, the box ends define 25th and 75th percentiles, whiskers define the 10th and 90th percentiles and outliners are dotted. References for mineral equilibrium constants are [1](Parkhurst, 2015), [2](Chaïrat et al., 2007a), [3](Blanc, 2015), [4](Al-Borno and Tomson, 1994), [5](Wagman et al., 1982), [6](Al et al., 2000), [7](Jahnke, 1984) and [8](Stumm and Morgan, 1996).

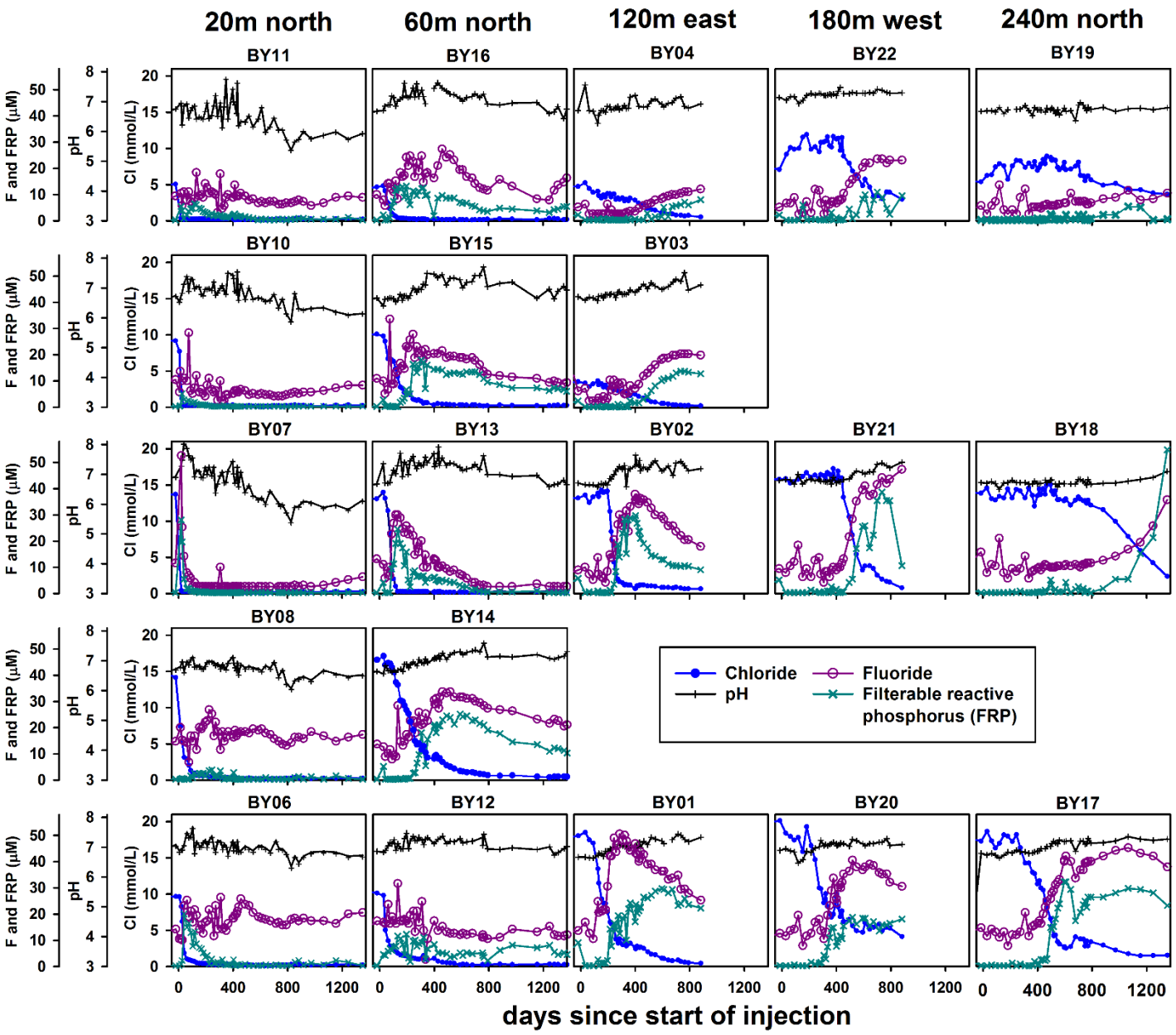


**Figure 4:** Observed breakthrough behaviour of chloride (Cl), pH, fluoride (F) and filterable reactive phosphorus (FRP) during the field injection experiment. Plots are arranged in columns representing monitoring bore nests at radial distances 20 m, 60 m, 120 m, 180 m and 240 m respectively from the injection well. See Figure 2 for location of screen intervals. Breakthrough of deionised wastewater is indicated by low chloride.

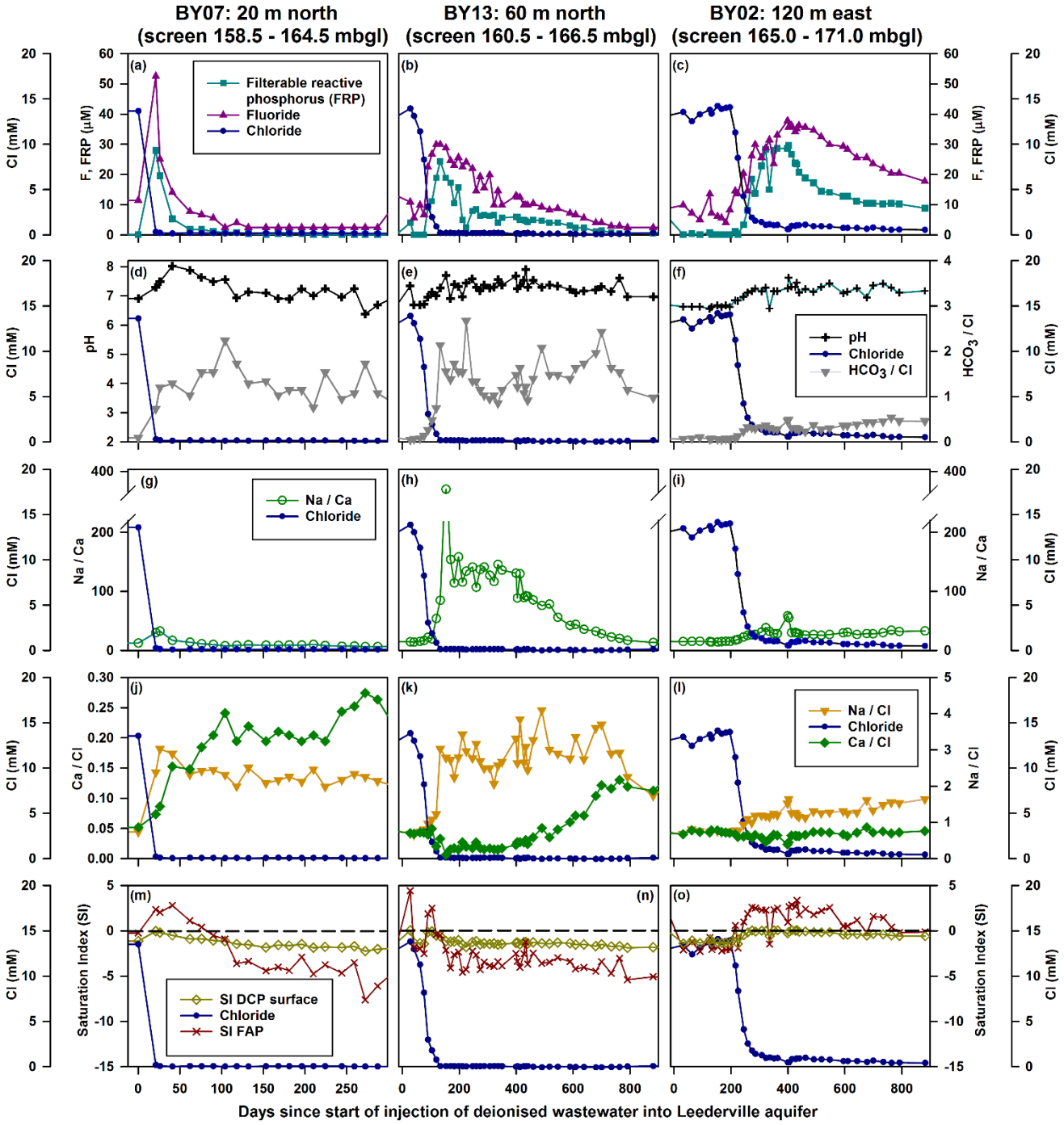


**Figure 5:** Observed ion ratios and SIs during breakthrough of deionised wastewater for selected wells BY07, BY13 and BY02: (a) – (c) chloride, fluoride and filterable reactive phosphate (FRP) (d) – (f) chloride, pH and $HCO_3$/Cl ratio (g) – (i) chloride and Na/Ca ratio (j) – (k) chloride, Na/Cl and Ca/Cl ratios (m) – (o) chloride, DCP surface SI and FAP SI.

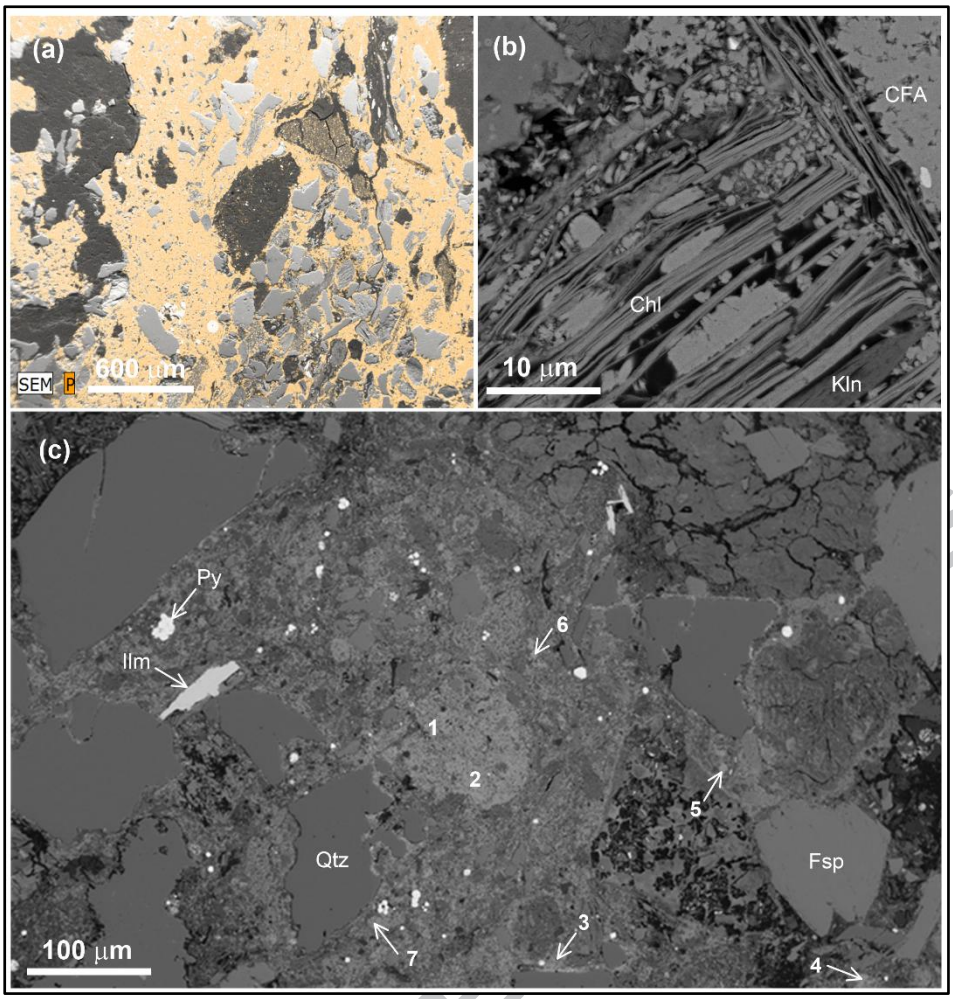


**Figure 6:** (a) SEM elemental mapping image of the CFA rich nodule. CFA marked orange (= phosphorous) occurs as cement infilling quartz and feldspar grains (grey colours). Black grains are undifferentiated mineral carbon. (b) High resolution SEM image showing micron sized CFA grains infilling chlorite (Chl) sheets and kaolinite (Kln) packets. (c) SEM image showing location of the microprobe analysis points (points 1 to 7) targeting dense areas of CFA cement. The CFA cement infills micropores between grains of quartz (Qtz), feldspar (Fld), illemite (Ilm) and pyrite (Py).

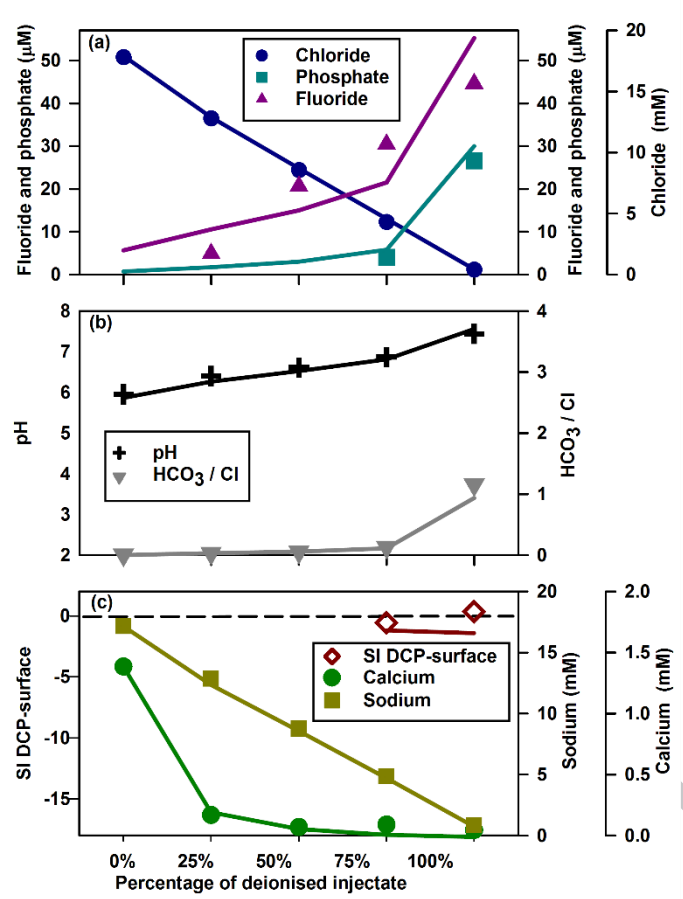


**Figure 7:** Solution evolution during anoxic experiment where CFA rich powder was mixed with different proportions of representative NGW and representative DeI solutions: (a) chloride, fluoride and phosphate (b) chloride, pH and $HCO_3^-/Cl^-$ ratio (c) sodium, calcium and SI DCP-surface. Average of two replicates (Table 3) are plotted. Laboratory results are indicated by symbols and model results are indicated by the solid lines.

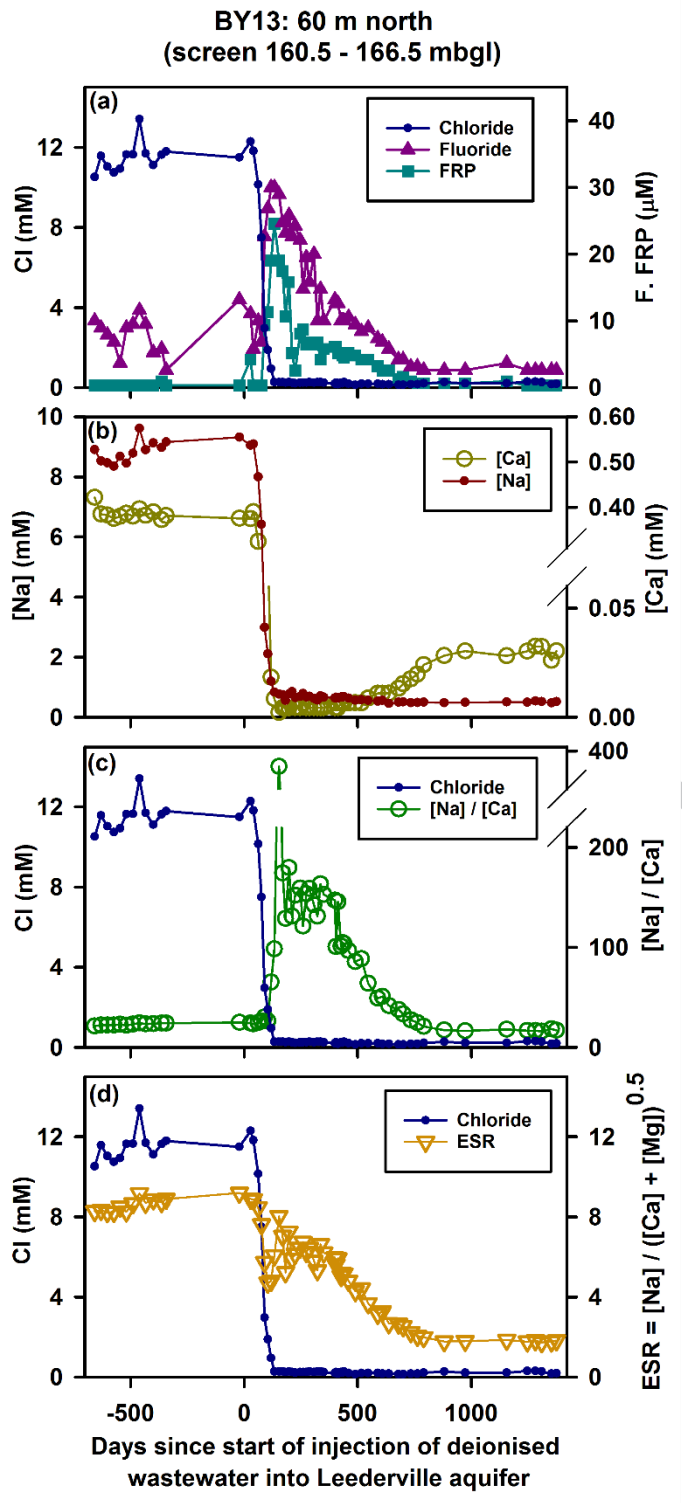


**Figure 8:** Observed sodium to calcium ratios relative to fluoride and phosphate release for monitoring well BY13: (a) chloride, fluoride and filterable reactive phosphorus (FRP) (b) sodium, calcium (c) sodium/calcium, chloride (d) Exchangeable sodium ratio = [Na] / ([Ca] + [Mg])$^{0.5}$, chloride. Square brackets indicate activities.

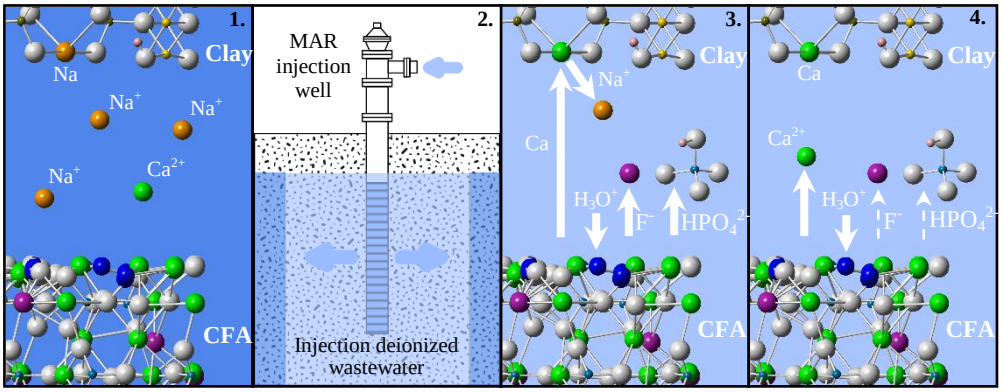

Highlights (3 to 5 bullet points, maximum 85 characters including spaces per bullet point)

- Fluoride and phosphate were mobilised during a MAR trial with deionised wastewater.
- CFA was identified as the source of fluoride and phosphate.
- Lab experiments with CFA rich nodules reproduced the field-observed behaviour.
- CFA and FAP are ubiquitous in many aquifer settings.
- F mobilisation risks need to be evaluated prior to MAR with low ionic strength water.